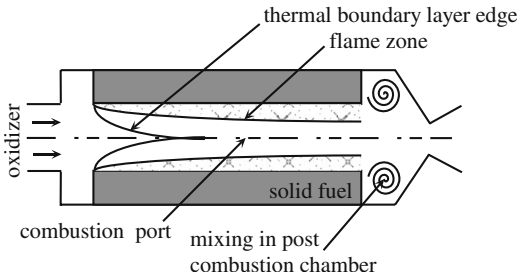

Fig. 1 Schematic of the circular-port hybrid rocket

partly accomplished by Majdalani and Saad [28] in a recent study of the Taylor–Culick profile with arbitrary headwall injection. However, their analysis was strictly focused on the construction of inviscid series approximations and computational verifications of the flow field with arbitrary headwall injection. Until more refined models become available, the idealization that we seek may be viewed as a first-cut, far field approximation due to the three main reasons that will be expounded next.

Unlike SRMs, the burning rate of hybrid rocket fuel is very sensitive to the flow field in the chamber [29,30]. Hence, many standard assumptions, such as uniform burning, which can be justified in SRMs, become less suitable in hybrids.

The validity of the inviscid solution for SRMs has been shown to be adequate at high injection Reynolds numbers, generally, exceeding 500 [14–17]; this is easily satisfied in SRMs where large burning rates produce Reynolds numbers in excess of 1000. In hybrid chambers, the fuel burning rate remains an order of magnitude smaller [31], albeit sufficiently large to justify an asymptotic treatment in which viscosity can be properly incorporated. The construction of a viscous solution appears to be more essential here than in the case of SRMs, especially that viscous effects will have a more pronounced impact on pressure than velocity. With this feature in mind, a viscous rotational approximation will be provided as a more accurate alternative.

The real challenge of hybrid propulsion stands in the mixing and burning of the two streams. However, in seeking a basic description, no attempts will be made to consider the mixing of the oxidizer and fuel or to model the burning of the two streams. These desirable pursuits will be deferred to later studies in which nonuniform burning, mixing, and the effect of particle-mean flow interactions may be separately addressed.

2 Hybrid Model

The basic hybrid engine can be modeled as a cylindrical chamber of porous length L and radius a with both a permeable head end and a fully open downstream end. The permeable head end permits the injection of a fluid at a prescribed velocity profile. A sketch of the chamber is given in Fig. 3 where $\bar{r}$ and $\bar{z}$ are used to denote the radial and axial coordinates. The field of interest extends from the head end to the nozzle's attachment point at the

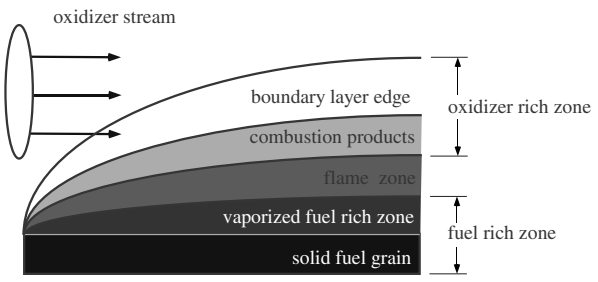

Fig. 2 Decreasing fuel concentration zones above solid surface during hybrid grain pyrolysis

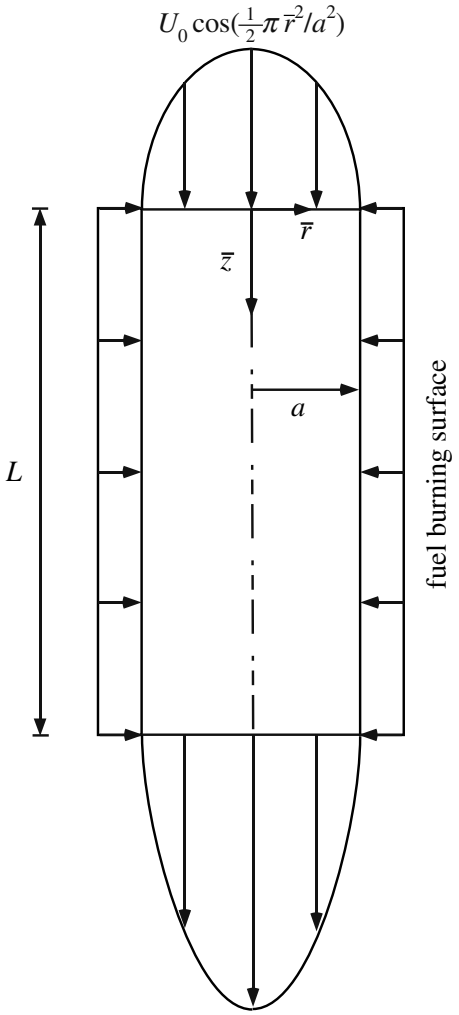

Fig. 3 Sketch of the rotational full-length hybrid model depicting mass addition along both sidewall and endwall boundaries. Here the oxidizer injection at the head end corresponds to a sinusoidal profile.

base of the chamber. Downstream of the base, the flow is accelerated after expanding through a nozzle whose treatment is not required here. This mathematical model does not take into account the three-dimensional complexity of the nozzle attachment, which will be highly variable depending on specific design shapes and nozzle types. In this vein, compressibility effects are discounted with the flow being controlled by conditions established upstream of the nozzle location. Using the present study as a starting point, a more elaborate model can be later constructed that would include nozzle effects, interactions with the flame sheet, etc.

At the head end, an oxidizer stream is injected into the chamber at a maximum centerline speed equal to U_0. This incoming oxidizer merges with the peripheral flux caused by uniform mass addition at the porous sidewall. The sidewall injection velocity U_w is used to represent the solid fuel regression rate. Clearly, U_w can be appreciably smaller than U_0 due to typical rates of fuel pyrolysis. This condition can be later exploited in seeking an asymptotic approximation of higher order. The current analysis seeks to capture the essential features of the ensuing flow field using a sinusoidal head end injection profile, namely,

$$\bar{u}_z(\bar{r},0) = U_0 \cos\left(\tfrac{1}{2}\pi \bar{r}^2/a^2\right) \tag{1}$$

The corresponding motion arises naturally due to the developing rotational flow field in a porous tube with normal sidewall mass addition [10,32].

2.1 Equations. A nonreactive flow can be considered, prompted by the low volumetric heat release that accompanies diffusion flames. Furthermore, the basic flow can be assumed to be (i) steady, (ii) incompressible, (iii) rotational, and (iv) axisymmetric. Based on these assumptions, the Navier–Stokes equations become

$$\frac{1}{\bar{r}}\frac{\partial(\bar{r}\bar{u}_r)}{\partial\bar{r}}+\frac{\partial\bar{u}_z}{\partial\bar{z}}=0 \tag{2}$$

$$\bar{u}_r\frac{\partial\bar{u}_r}{\partial\bar{r}}+\bar{u}_z\frac{\partial\bar{u}_r}{\partial\bar{z}}=-\frac{1}{\rho}\frac{\partial\bar{p}}{\partial\bar{r}}+\nu\left[\frac{\partial^2\bar{u}_r}{\partial\bar{z}^2}+\frac{\partial}{\partial\bar{r}}\left(\frac{1}{\bar{r}}\frac{\partial(\bar{r}\bar{u}_r)}{\partial\bar{r}}\right)\right] \tag{3}$$

$$\bar{u}_r\frac{\partial\bar{u}_z}{\partial\bar{r}}+\bar{u}_z\frac{\partial\bar{u}_z}{\partial\bar{z}}=-\frac{1}{\rho}\frac{\partial\bar{p}}{\partial\bar{z}}+\nu\left[\frac{\partial^2\bar{u}_z}{\partial\bar{z}^2}+\frac{1}{\bar{r}}\frac{\partial}{\partial\bar{r}}\left(\bar{r}\frac{\partial\bar{u}_z}{\partial\bar{r}}\right)\right] \tag{4}$$

Note that the effect of the wall regression on the mean flow is neglected in most analyses of SRMs [19,20]. It can be safely ignored in the case of hybrids due to their relatively slower regression.

2.2 Boundary Conditions. The boundary conditions are due to symmetry, no slip at the sidewall, and both head end and sidewall injection. Specifically, one can assume

(a) uniform injection along the cylindrical sidewall,
(b) vanishing axial flow in fulfillment of the no slip boundary condition at the sidewall,
(c) a prescribed injection pattern at the head end and
(d) vanishing radial velocity along the centerline.

These particulars can be written as

$$\begin{cases}\bar{r}=a, & 0\le\bar{z}<L, \quad \bar{u}_r=-U_w \quad \text{(sidewall injection)}\\ \bar{r}=a, & 0\le\bar{z}<L, \quad \bar{u}_z=0 \quad \text{(no slip at the wall)}\\ \bar{z}=0, & \forall\,\bar{r}, \quad \bar{u}_z=U_0\cos\left(\frac{1}{2}\pi\bar{r}^2/a^2\right) \quad \text{(endwall)}\\ \bar{r}=0, & \forall\,\bar{z}, \quad \bar{u}_r=0 \quad \text{(no flow across centerline)}\end{cases} \tag{5}$$

2.3 Normalization. In seeking a similarity solution, it is helpful to normalize all variables and operators. This can follow

$$z=\frac{\bar{z}}{a}, \quad r=\frac{\bar{r}}{a}, \quad \nabla=a\bar{\nabla}, \quad p=\frac{\bar{p}}{\rho U_w^2} \tag{6}$$

$$u_r=\frac{\bar{u}_r}{U_w}; \quad u_z=\frac{\bar{u}_z}{U_w}; \quad u_0=\frac{U_0}{U_w} \tag{7}$$

Here $U_0=\bar{u}_z(0,0)$ and $U_w=-\bar{u}_r(a,\bar{z})$ represent the maximum fluid injection velocity at the head end and the uniform wall injection velocity at the sidewall, respectively. The corresponding boundary conditions reduce to

$$\begin{cases}u_r(1,z)=-1\\ u_z(1,z)=0\\ u_z(r,0)=u_0\cos\left(\frac{1}{2}\pi r^2\right)\\ u_r(0,z)=0\end{cases} \tag{8}$$

At this point, the vorticity transport equation, $\nabla\times\boldsymbol{u}\times\boldsymbol{\Omega}=\mathbf{0}$, may be solved in conjunction with the constraints granted by Eq. (8).

2.4 Rotational Solution. For a sinusoidal head end injection velocity, the vorticity stream function approach can be applied by introducing

$$u_r=-\frac{1}{r}\frac{\partial\psi}{\partial z} \quad u_z=\frac{1}{r}\frac{\partial\psi}{\partial r} \tag{9}$$

Substitution into $\nabla\times\boldsymbol{u}\times\boldsymbol{\Omega}=\mathbf{0}$ yields

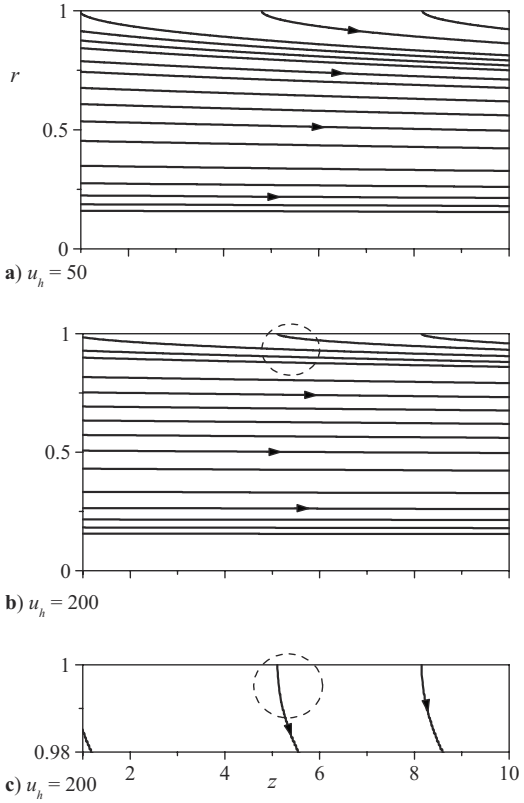

Fig. 4 Rotational streamlines shown for two increasing head end injection parameters. The inset in part (*c*) corresponds to a magnified section of part (*b*) illustrating the normal sidewall injection feature.

$$\frac{\partial\psi}{\partial z}\frac{\partial}{\partial r}\left(\frac{\Omega_\theta}{r}\right)=\frac{\partial\psi}{\partial r}\frac{\partial}{\partial z}\left(\frac{\Omega_\theta}{r}\right), \quad \Omega_\theta=\frac{\partial u_r}{\partial z}-\frac{\partial u_z}{\partial r} \tag{10}$$

This expression will be satisfied when $\Omega_\theta/r=F(\psi)$. In seeking a closed-form solution, we insert $\Omega_\theta=C^2r\psi$ into the vorticity equation and collect

$$\frac{\partial^2\psi}{\partial z^2}+\frac{\partial^2\psi}{\partial r^2}-\frac{1}{r}\frac{\partial\psi}{\partial r}+C^2r^2\psi=0 \tag{11}$$

Similarly, the boundary conditions may be written for the stream function. Based on Eq. (8), we have

$$\begin{cases}\frac{1}{r}\frac{\partial\psi(1,z)}{\partial z}=-1, & \frac{1}{r}\frac{\partial\psi(1,z)}{\partial r}=0\\ \frac{1}{r}\frac{\partial\psi(r,0)}{\partial r}=u_0\cos\left(\frac{1}{2}\pi r^2\right), & \frac{1}{r}\frac{\partial\psi(0,z)}{\partial z}=0\end{cases} \tag{12}$$

Then using separation of variables, we let $\psi(r,z)=f(r)g(z)$ and reduce Eq. (11) into

$$-\frac{g''}{g}=\frac{f''}{f}-\frac{1}{r}\frac{f'}{f}+C^2r^2=\pm\lambda^2 \tag{13}$$

One may infer from Eq. (12) that the derivative of $g(z)$ must be a constant to ensure a linear variation in z. The case of $\lambda=0$ is selected, thus leading to $f=A\cos\left(\frac{1}{2}Cr^2\right)+B\sin\left(\frac{1}{2}Cr^2\right)$ and $g=C_1z+C_2$. Subsequent application of Eq. (12) produces, systematically, $A=0$, $B=C_1^{-1}$, $C=\pi$, and $C_2=C_1u_0/\pi$. At length, we recover

$$\psi=(z+u_h)\sin\left(\frac{1}{2}\pi r^2\right), \quad u_h\equiv u_0/\pi \tag{14}$$

As shown in Fig. 4, increasing the headwall injection parameter increases the flow turning severity near the sidewall. Specifically,

as u_h is increased from 50 to 200, the streamlines, which otherwise resemble those of a solid rocket motor, become dominated by axial (parallel-flow) motion everywhere except in the neighborhood of the sidewall. This can be clearly attributed to the increased propensity of the axial stream flowing into the chamber. At larger u_h the normally injected stream is met by an overwhelmingly larger axial flow that forces it to rapidly turn and assimilate with it. In practice, the values of U_0 and U_w can be calibrated to reproduce the patterns associated with a prototypical hybrid engine.

Based on Eq. (14), other pertinent variables may be evaluated. For example, one finds

$$u_r = -\frac{1}{r}\sin\left(\tfrac{1}{2}\pi r^2\right), \quad u_z = \pi(z+u_h)\cos\left(\tfrac{1}{2}\pi r^2\right),$$
$$\Omega_\theta = \pi^2(z+u_h)r\,\sin\left(\tfrac{1}{2}\pi r^2\right) \tag{15}$$

$$\frac{\partial p}{\partial r} = -\frac{-1+\pi r^2\sin(\pi r^2)+\cos(\pi r^2)}{2r^3}, \quad \frac{\partial p}{\partial z} = -\pi^2(u_h+z) \tag{16}$$

and, for the pressure drop from the head end, one can put

$$\Delta p = \frac{-1-2\pi^2 r^2 z(2u_h+z)+\cos(\pi r^2)}{4r^2} \tag{17}$$

In Fig. 5, the two velocity components, vorticity and the radial pressure drop at the head end, are plotted. While the axial velocity increases linearly with the head end injection parameter, the radial velocity remains unaffected. In fact, the radial component is seen to be identical to its counterpart in SRMs, namely, that of Culick [9]. In Fig. 5(*c*), the vorticity is seen to be largest near the sidewall where flow is entering perpendicularly to the fuel surface. Away from the wall, vorticity decays rapidly; it approaches zero near the centerline where the flow becomes nearly uniform. As for the pressure drop, Fig. 5(*d*) illustrates how $\Delta p(r,0)$ in the head end plane can surpass its wall value when

$$\tfrac{1}{2}\sqrt{2} < r < 1 \tag{18}$$

In this range, the largest magnitude corresponds to $\Delta p = -0.569108$. This extremum corresponds to $r_m = 0.861405$ and can be obtained by differentiating Eq. (17) at fixed z. Note that the radial pressure variation is strongly connected with the radial velocity shown in Fig. 5(*b*). Both experience an unexpected surge in magnitude immediately after injection, thus exceeding their absolute value at the wall.

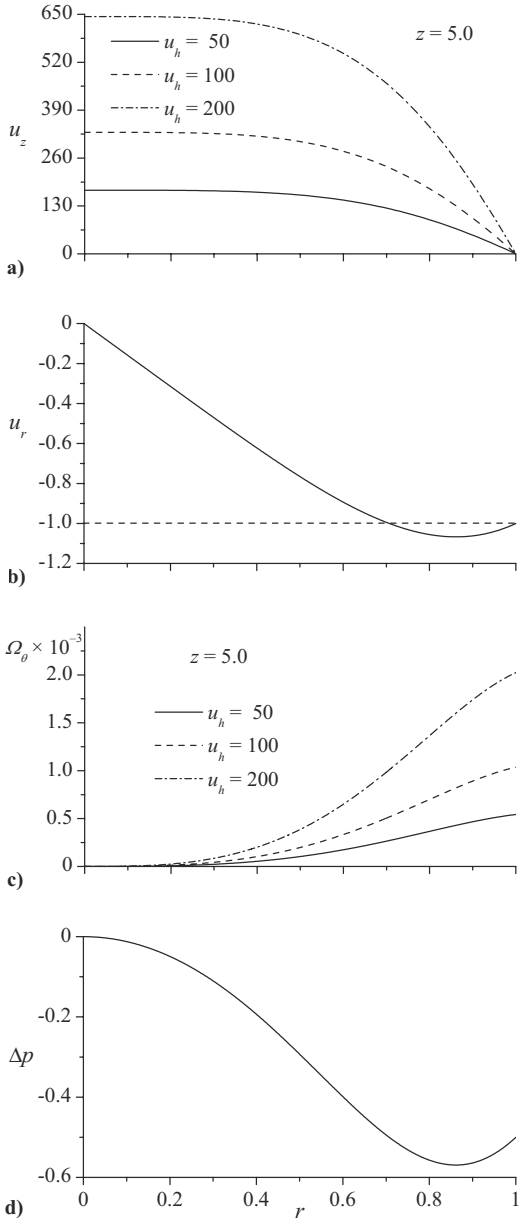

Fig. 5 Description of (*a*) axial and (*b*) radial velocities in addition to (*c*) vorticity and (d) pressure drop at the chamber's head end. Both axial velocity and vorticity are shown at a fixed axial position.

3 Viscous Rotational Solution

Viscous effects can be accommodated, as performed previously in the context of SRM internal ballistics by Majdalani and coworkers [19,20]. To that end, one can start with the reduced Navier–Stokes equation incorporating both viscosity and wall regression speed. Then by putting $\alpha = 0$ in Refs. [19,20], we are left with the case corresponding to stationary walls, namely,

$$2\varepsilon\left(\theta\frac{\mathrm{d}^4F}{\mathrm{d}\theta^4}+2\frac{\mathrm{d}^3F}{\mathrm{d}\theta^3}\right)+F\frac{\mathrm{d}^3F}{\mathrm{d}\theta^3}-\frac{\mathrm{d}F}{\mathrm{d}\theta}\frac{\mathrm{d}^2F}{\mathrm{d}\theta^2}=0 \tag{19}$$

where

$$\psi = \frac{\bar{\psi}}{a^2U_w} = (z+u_h)F, \quad u_r = -\frac{F}{r}, \quad u_z = \frac{(z+u_h)}{r}\frac{\mathrm{d}F}{\mathrm{d}r} \tag{20}$$

The corresponding boundary conditions are

$$\frac{\mathrm{d}F\left(\frac{1}{2}\pi\right)}{\mathrm{d}\theta}=0, \quad F\left(\tfrac{1}{2}\pi\right)=1, \quad F(0)=0, \quad \lim_{\theta\to 0}\sqrt{\theta}\frac{\mathrm{d}^2F}{\mathrm{d}\theta^2}=0 \tag{21}$$

Note that $\varepsilon \equiv \nu/(aU_w)$ is the inverted Reynolds number based on the wall injection velocity.

Equation (19) may be solved asymptotically by first setting $F = F_0 + \varepsilon F_1 + O(\varepsilon^2)$ and then inserting the expanded form back into Eq. (19). At the leading order, one retrieves

$$F_0\frac{\mathrm{d}^3F_0}{d\theta^3}-\frac{\mathrm{d}F_0}{\mathrm{d}\theta}\frac{\mathrm{d}^2F_0}{\mathrm{d}\theta^2}=0 \tag{22}$$

where $F_0 = \sin\theta$ represents a suitable outcome. The first order equation becomes

$$\frac{d^3F_1}{d\theta^3}\sin\theta-\frac{d^2F_1}{d\theta^2}\cos\theta+\frac{dF_1}{d\theta}\sin\theta-F_1\cos\theta=-2\theta\sin\theta \tag{23}$$

To solve Eq. (23), one can apply the variation of parameters approach twice in succession. To this end, a homogenous solution is introduced in the form of $F_{1h}=C(\theta)\cos\theta$, where $C(\theta)$ is a variable coefficient. Through backward substitution into Eq. (23), one collects

$$C'''\sin\theta\cos\theta-2C''\sin^2\theta-C''=0 \tag{24}$$

whence

$$C(\theta)=K_0\tan\theta+K_1\theta+K_2 \tag{25}$$

With $C(\theta)$ in hand, the homogenous part becomes

$$F_{1h}=K_0\sin\theta+K_1\theta\cos\theta+K_2\cos\theta \tag{26}$$

At this point, the method of variation of parameters is applied a second time by permitting K_0, K_1, and K_2 to vary in space. Consequently, Eq. (26) is rewritten as

$$F_1(\theta)=K_0(\theta)\sin\theta+K_1(\theta)\theta\cos\theta+K_2(\theta)\cos\theta \tag{27}$$

Then using Eq. (23), one recovers

$$K_0'\sin\theta+K_1'\theta\cos\theta+K_2'\cos\theta=0 \tag{28}$$

$$K_0'\cos\theta+K_1'(\cos\theta-\theta\sin\theta)-K_2'\sin\theta=0 \tag{29}$$

and

$$-K_0'\sin^2\theta-K_1'(2\sin^2\theta+\theta\cos\theta\sin\theta)-K_2'\cos\theta\sin\theta=4\cos\theta-2\theta\sin\theta \tag{30}$$

The ensuing set of coupled, first order ordinary differential equations (ODEs) may be solved to obtain

$$K_0=-2\csc\theta-\sin\theta-\theta\cos\theta-S(\theta)+C_0 \tag{31}$$

$$K_1=2\csc\theta+S(\theta)+C_1 \tag{32}$$

$$K_2=-\cos\theta+\theta\sin\theta-2\theta\csc\theta-S_1(\theta)+C_2 \tag{33}$$

where

$$S(\theta)=\int_0^\theta\phi\csc\phi\,\mathrm{d}\phi=\theta+\sum_{k=1}^{\infty}\frac{2}{\pi^{2k}}\left(\sum_{n=1}^{\infty}\frac{1}{n^{2k}}\right)\frac{(1-2^{1-2k})}{(2k+1)}\theta^{2k+1} \tag{34}$$

$$S_1(\theta)=\int_0^\theta\phi^2\csc\phi\,\mathrm{d}\phi=\frac{1}{2}\theta^2+\sum_{k=1}^{\infty}\left(\sum_{n=1}^{\infty}n^{-2k}\right)\frac{(1-2^{1-2k})}{(k+1)\pi^{2k}}\theta^{2k+2} \tag{35}$$

Thus, by combining the leading and first order solutions, a complete viscous approximation may be expressed as

$$F=\sin\theta+\varepsilon\{-3+(\theta\cos\theta-\sin\theta)S(\theta)-S_1(\theta)\cos\theta+C_0\sin\theta+C_1\theta\cos\theta+C_2\cos\theta\} \tag{36}$$

where

$$C_0=3+S\left(\tfrac{1}{2}\pi\right),\quad C_1=-6\pi^{-1}-1-S\left(\tfrac{1}{2}\pi\right)+(2/\pi)S_1\left(\tfrac{1}{2}\pi\right),\quad C_2=3 \tag{37}$$

By inspection, it can be seen that, if viscosity is set to zero in Eq. (36), the inviscid form given by Eqs. (14) and (15) will be recovered. In summary, the viscous approximation for the rotational model comprises

$$\psi=(z+u_h)\Big[\sin\theta+\varepsilon\Big(-3+\Big[3+S\left(\tfrac{1}{2}\pi\right)-S(\theta)\Big]\sin\theta-\cos\theta\Big\{S_1(\theta)-3+\theta\Big[1+6\pi^{-1}+S\left(\tfrac{1}{2}\pi\right)-S(\theta)-2\pi^{-1}S_1\left(\tfrac{1}{2}\pi\right)\Big]\Big\}\Big)\Big]+O(\varepsilon^2) \tag{38}$$

$$u_r=-\sqrt{\frac{\pi}{2\theta}}\Big[\sin\theta+\varepsilon\Big(-3+\Big[3+S\left(\tfrac{1}{2}\pi\right)-S(\theta)\Big]\sin\theta-\cos\theta\Big\{S_1(\theta)-3+\theta\Big[1+6\pi^{-1}+S\left(\tfrac{1}{2}\pi\right)-S(\theta)-2\pi^{-1}S_1\left(\tfrac{1}{2}\pi\right)\Big]\Big\}\Big)\Big]+O(\varepsilon^2) \tag{39}$$

$$u_z=\pi(z+u_h)\Big[\cos\theta+\varepsilon\Big(-\theta+2\Big[1-2\pi^{-1}+\pi^{-1}S_1\left(\tfrac{1}{2}\pi\right)\Big]\cos\theta+\Big\{S_1(\theta)-3+\theta\Big[1+6\pi^{-1}+S\left(\tfrac{1}{2}\pi\right)-S(\theta)-2\pi^{-1}S_1\left(\tfrac{1}{2}\pi\right)\Big]\Big\}\sin\theta\Big)\Big]+O(\varepsilon^2) \tag{40}$$

As for the corrected pressure drop, it can be obtained by integrating from the centerline to any radius. One gets

$$\begin{aligned}\Delta p_\perp\equiv p(0,z)-p(\theta,z)&=\pi\left[\varepsilon F_\theta+\tfrac{1}{4}\theta^{-1}F^2-\varepsilon F_\theta(0)\right]\\&=\tfrac{1}{4}\pi\theta^{-1}\sin^2\theta+\varepsilon\pi\Big(\cos\theta-1-\tfrac{3}{2}\theta^{-1}\sin\theta\\&\quad+\tfrac{1}{4}\theta^{-1}\Big\{3+S\left(\tfrac{1}{2}\pi\right)-S(\theta)+\cos(2\theta)\Big[S(\theta)-S\left(\tfrac{1}{2}\pi\right)-3\Big]\Big\}\\&\quad+\tfrac{1}{4}\sin(2\theta)\Big\{S(\theta)-S\left(\tfrac{1}{2}\pi\right)-1-6\pi^{-1}+2\pi^{-1}S_1\left(\tfrac{1}{2}\pi\right)\\&\quad+\theta^{-1}[3-S_1(\theta)]\Big\}+O(\varepsilon^2)\end{aligned} \tag{41}$$

In like fashion, the pressure drop in the flow direction can be estimated from

$$\begin{aligned}\Delta p_\parallel\equiv p(\theta,0)-p(\theta,z)&=-\pi^2z\left(\tfrac{1}{2}z+u_h\right)[2\varepsilon(\theta F_{\theta\theta\theta}+F_{\theta\theta})-(F_\theta)^2+FF_{\theta\theta}]\\&=\pi^2z\left(\tfrac{1}{2}z+u_h\right)\{1+(2\varepsilon/\pi)[2\pi-6+4\pi\mathcal{C}-7\zeta(3)]\}+O(\varepsilon^2)\end{aligned} \tag{42}$$

where $\mathcal{C}=\frac{1}{2}S\left(\frac{1}{2}\pi\right)\approx0.91596559$ is Catalan's constant, and $\zeta(3)\approx1.2020569$ is the Riemann zeta function defined by $\zeta(x)=\sum_{k=1}^{\infty}k^{-x}$. Hence, one can put $\Delta p_\parallel\approx\pi^2z\left(\frac{1}{2}z+u_h\right)(1+2.15123\varepsilon)+O(\varepsilon^2)$. Finally, the shear stress (or vorticity) can be calculated from

$$\tau=\frac{\bar{\tau}}{\rho U_w^2}=-\varepsilon\Omega=\varepsilon z\sqrt{2}\pi^{3/2}\sqrt{\theta}F_{\theta\theta}=-\varepsilon z\sqrt{2}\pi^{3/2}\sqrt{\theta}\sin\theta+(O\varepsilon^2) \tag{43}$$

At the wall, one is left with $\tau_w=-\varepsilon z\pi^2+O(\varepsilon^2)$.

The viscous solution presented above is the result of a similarity transformation in space and time. Results, obtained using this approach, are illustrated in Fig. 6 at several Reynolds numbers ranging from 5 to ∞ (for inviscid conditions). The three parts in Fig. 6 correspond to the main characteristic function F, as well as both axial and radial velocities. Note that the influence of viscous damping is most pronounced near the centerline, as reflected in the flow smoothening or laminarization affecting the axial velocity in Fig. 6(*b*). This may also explain the steeper top-hat profiles associated with the inviscid solution. The characteristic function F and the radial velocity undergo a similar, albeit less appreciable flattening process.

In Fig. 7, the first order correction function F_1 is compared with two existing solutions developed, first, by Yuan and Finkelstein [33] and, second, by Terrill and Thomas [34]. These are derived in the context of a porous cylinder with stationary walls. For the Yuan–Finkelstein expression, we have